Variable resolution for SPH in three dimensions: Towards optimal splitting and coalescing for dynamic adaptivity

Variable resolution for SPH in three dimensions: towards optimal splitting and coalescing for dynamic adaptivity

R. Vacondio[a,*], B.D. Rogers[b], P.K. Stansby[b], P. Mignosa[a]

[a] *DICATeA, University of Parma, v.le G. Usberti 181/A, 43124 Parma, Italy*
[b] *Modelling and Simulation Centre, School of Mechanical, Aerospace and Civil Engineering, The University of Manchester, Manchester, M13 9PL, UK*

Abstract

As smoothed particle hydrodynamics (SPH) becomes increasingly popular for complex flow analysis the need to improve efficiency particularly for 3-D problems is becoming greater. Automatic adaptivity with variable particle size is therefore desirable. In this paper, a novel 3-D splitting and coalescing algorithm is developed which minimises density error while conserving both mass and momentum using a variational principle. Accuracy is increased in refined areas unaffected by coarser particle distributions elsewhere. For particle splitting, the key criteria are the number of split (daughter) particles, their distribution, spacing and kernel size. Four different splitting arrangements are investigated including a cubic stencil with 8 particles, a cubic stencil with an additional 6 located at the face centres, an icosoahedron-shaped arrangement with 14 particles, and a dodecahedron-shaped arrangement with 20 particles where particles are located at the vertices. The error analysis also examines whether retaining a particle at the centre of the arrangement is necessary revealing that regardless of the stencil adopted, to minimize the density error a daughter particle should be placed at the same position of the original particle. The optimum configuration is found to be the iconsahedron-shaped arrangement while commonly used smoothing kernels such as the cubic and quintic splines and Wendland produce similar density

*Corresponding author

Email addresses: renato.vacondio@unipr.it (R. Vacondio), benedict.rogers@manchester.ac.uk (B.D. Rogers), p.k.stansby@manchester.ac.uk (P.K. Stansby), paolo.mignosa@unipr.it (P. Mignosa)

errors, so that the optimal refinement stencil is effectively independent of the kernel choice. A new 3-D coalescing scheme completes the algorithm such that the particle resolution can be either increased or reduced locally. The SPH splitting and coalescing scheme, is tested with Poiseuille flow showing negligible loss of convergence accuracy in the refined area and the lid driven cavity for a wide range of Reynolds number showing good agreement with reference solutions again with local accuracy defined by particle distribution.

Keywords: Smoothed Particle Hydrodynamics, SPH, Meshfree methods, Navier-Stokes, Incompressible flow, splitting, coalescing, merging, adaptivity, refinement

---

1. Introduction

In mature numerical schemes variable resolution is adopted in order to improve the efficiency of the simulation without reducing the accuracy. In particular in Eulerian schemes different approaches are available in literature such as unstructured grids [6], Adaptive Mesh Refinement (AMR) based on octree grids [15], etc. Adaptivity is more difficult to achieve in SPH due to the Lagrangian nature of the method. In AMR schemes, the refinement pattern is strongly influenced or dictated by the shapes of individual mesh elements (triangular, tetrahedral, cubic) and by the data structure of the mesh-based technique (structured, unstructured, hierarchical). In a particle method such as SPH, the particles are moving and located in a non-uniform and irregular distribution with a far larger number of interacting neighbours making identification of the optimal particle splitting stencil less straightforward. Previous works in SPH have introduced variable resolution by either remeshing, and particle insertion/removal techniques [3, 9], dynamically varying particle characteristics [21], or through variable smoothing lengths with dynamic particle splitting and coalescing according to pre-defined criteria [23, 22]. In the Finite Volume Particle Method multi-resolution by Eulerian particles for high resolution zones[17] has been used. Only recently have schemes appeared that offer both runtime particle splitting and coalescing to provide dynamic adaptive resolution [2, 18, 23, 20]. Feldman and Bonet [5] defined the refinement stencil that should be used for 2-D models, however all those previous works are developed considering 2-D schemes whereas little attention has been dedicated to 3-D. Indeed, no work to date has investigated the optimal refinement stencil for 3-D variable resolution. 3-D stencils cannot be

generated by simply extending those obtained in 2D. Instead they have to be created in such a way that a negligible global density error is obtained with a minimum number of particles arranged in a spherically symmetric pattern.
The aim of this work is to develop a 3-D particle refinement scheme that includes both dynamic particle splitting and coalescing that minimises error within a SPH simulation.
In this work the global density error minimization algorithm has been extended to 3-D to define the position, smoothing length and other physical quantities of each daughter particle. Four different splitting patterns have been considered: cubic, cubic with additional particles located in the centre of the faces, icosahedron and dodecahedron. An accuracy analysis of how the daughter particle positions and smoothing lengths affect the global density error and the mass distribution has been conducted for each refinement pattern. Finally the optimal refinement pattern for 3-D simulations is identified. Both the Wendland and the cubic-spline kernels have been used to demonstrate that the analysis is independent of the choice of kernel.
While necessary to provide fine resolution, splitting particles leads to an eveer increasing number of particles. In previous papers [22, 23], we presented the first algorithm for SPH to coalesce or merge particles while minimising the error in density. Here we extend that methodology to 3-D to reduce the number of particles during a simulation automatically where high resolution is no longer necessary.
Mass and momentum conservation, also in the presence of particles with variable mass and smoothing length is guaranteed by using a weakly compressible variationally consistent SPH algorithm. The numerical scheme has been developed by extending the capability of the parallelSPHysics open-source software (www.sphysics.org).
To increase the accuracy a particle shifting correction [19] has been used in the update of the particle position, and an additional diffusion term has been added to the continuity equation [11].
This paper is structured as follows: in the next section the splitting procedure is presented with the optimal refinement pattern investigated. This is followed by Section 3, where we present the procedure for particle coalescing (merging). In Section 4, we present the variationally consistent SPH formulation for variable resolution and then we present 3-D validation cases in Section 5.

2. SPH Interpolation and Approximation

Before developing the error minimisation approach for 3-D splitting of SPH particles, we first introduce the basic SPH discrete interpolation.

2.1. SPH procedure

The SPH method uses a local summation procedure with surrounding particles to perform a local interpolation. A function f can be approximated according to:

$$\langle f \rangle_i = \sum_j^N f_j W_i(\mathbf{x}_j, h) V_j \tag{1}$$

where $\langle \cdot \rangle$ denotes the SPH approximation, V_j and f_j are the volume and value of f of the jth particle respectively, the smoothing length h is the parameter that determines the size of the support for the weighting function, $W(\mathbf{x} - \mathbf{x}', h)$ and N is the number of particles inside the compact support of particle i.

In Vacondio et al. [22], we showed that the most accurate procedure for variable resolutions simulations as presented herein, was to use a scatter formulation where the kernel is evaluated using the smoothing length of the surrounding particles, h_j. Hernquist & Katz [8] have shown that both scatter and gather formulations have the same order of convergence and produce similar errors. The SPH scatter interpolation of a generic scalar function f is:

$$\langle f_i \rangle = \sum_{j=1}^N f_j W_i \left(\mathbf{x}_j, h_j\right) V_j \tag{2}$$

The local density is therefore defined using a scatter formulation at a generic point x:

$$\rho\left(\mathbf{x}\right) = \sum_{j=1}^N m_j W_j \left(\mathbf{x}, h_j\right) \tag{3}$$

where m_j is the mass of the jth particle. This estimation of the density can then be used as the basis for an error minimisation analysis when identifying the optimal splitting pattern.

3. Particle splitting

3.1. Splitting procedure

To increase the resolution in certain areas of the domain one original particle N is split into M_S daughter particles. The mass m_k, position $\mathbf{x}_k$, velocity vector $\mathbf{v}_k$, and smoothing length h_k for any of the $k = 1...M_S$ refined particles must be defined, therefore the total number of degrees of freedom is 8 (in 3-D) for each k-th daughter particle. To reduce the degrees of freedom of the problem, the number of new particles M_S and their relative positions are given by using a fixed regular refinement pattern, which defines the relative position of daughter particles. The distance between the original particles and the daughter ones is defined as $\epsilon \cdot h_N$, where ϵ is a non-dimensional coefficient and h_N the smoothing length of the original particle N. Please note that the coefficient ϵ defines the relative position of the daughter particles for a given spherically symmetric stencil. Once the refinement pattern is defined, the smoothing lengths of the daughter particles are calculated as $h_k = \alpha h$ where α is a scalar parameter called the smoothing ratio. The basic idea of this procedure, is to fix arbitrarily the parameters ϵ and α and then obtain the masses of the daughter particles m_k *prior to simulation* by minimizing the global error between the refined $\rho(\mathbf{x})$ and unrefined $\rho^*(\mathbf{x})$ density, defined as [5]:

$$\mathscr{E} = \int_{\Omega} e\left(\mathbf{x}\right)^2 d\mathbf{x} \tag{4}$$

where Ω is the domain, and $e(\mathbf{x}) = \rho^*(\mathbf{x}) - \rho(\mathbf{x})$
The density ρ is calculated using a scatter density formulation [8]:

$$\rho_i = \sum_j m_j W_i(\mathbf{x}_j, h_j) \tag{5}$$

where m is the mass, and $W_i(\mathbf{x}_j, h_j)$ is the kernel function with smoothing length h. After some algebra [24] it is possible to define the following minimization problem:

$$\mathscr{E}^* = \min_{\boldsymbol{\lambda}} \left\{ \overline{C} - 2\boldsymbol{\lambda}^T \overline{\mathbf{b}} + \boldsymbol{\lambda}^T \overline{\mathbf{Q}} \boldsymbol{\lambda} \right\} \tag{6}$$

where $\mathscr{E}^*$ is the global minimum density error, and:

$$\lambda_k = \frac{m_k}{m_N}$$

$$\overline{C} = \int_\Omega W_N^2\left(\mathbf{x}, h_N\right) d\mathbf{x}$$

$$\overline{b}_k = \int_\Omega W_N\left(\mathbf{x}, h_N\right) W_k\left(\mathbf{x}, h_k\right) d\mathbf{x}$$

$$\overline{Q}_{lk} = \int_\Omega W_k\left(\mathbf{x}, h_k\right) W_l\left(\mathbf{x}, h_l\right) d\mathbf{x}$$

Moreover due to mass conservation, the following constraint in the minimization problem holds:

$$\sum_{k=1}^{M_S} \lambda_k = 1 \tag{7}$$

The global density error $\mathscr{E}^*$ depends on the choice of the refinement parameters α and ϵ and on the vector of coefficients $[\lambda_1 ... \lambda_{M_S}]$. Therefore it is independent of the initial mass m_N, smoothing length h_N and of the other particle positions. Hence, it is possible to define the optimal mass distribution before the beginning of the simulation by solving the model problem of Equations (6) with the constraint (7).
We remark here that fluid particles are split during the simulation when they enter high-resolution regions, however the relative position and mass of the daughter particles are calculated before the simulation starts following the procedure explained above. In this way solving a computationally expensive minimization problem during the simulation is avoided and this guarantees that the computational costs generated by the particle splitting procedure are minimal.

3.2. Analysis of different refinement patterns

In 2D it has been demonstrated that the hexagonal refinement pattern is a good balance between the total number of particles and the reduction of the density error [5, 24, 23, 22]. The aim of the present work is to analyse different 3-D refinement patterns and identify the optimal arrangement.
In particular the following patterns have been analysed:

- cubic (8 particles, figure 1-a),

- cubic with 6 additional particles located on the sphere circumscribed around the cubic and located along the line passing through the face centres (14 particles, figure 1-b),
- icosahedron (12 particles, figure 1-c),
- dodecahedron (20 particles, figure 1-d)

In all configurations one additional daughter particle can be located in the centre of the 3-D geometrical figure, at the position of the original particle N. All particle splitting patterns with a daughter particle at the centre are referred to using a "+1 ". For example, the cubic stencil without a daughter particle at the centre is referred to as "cubic ", while with the daughter particle at the centre is referred to as "cubic+1 "

For each refinement pattern the variation of the global minimum density error $\mathscr{E}^*$ has been calculated varying ϵ and α between 0.3 and 0.9 with steps of 0.01. In this way the density error contours shown in Figure 2 have been obtained using the Wendland kernel. Please note also that from the procedure described in Section 3 the daughter particles might have a different mass because the values of $[\lambda_1 ... \lambda_M]$ are not imposed but obtained from the minimization problem. However, due to the fact that we have analysed refinement patterns with spherical symmetry, the daughter particles located at the vertices have the same mass, so only the particle in the centre might have a different mass.
The ratio between the maximum and the minimum mass of the daughter particles $\lambda_{min}/\lambda_{max}$ are plotted in Figure 2. The contour lines of $\lambda_{min}/\lambda_{max} < 0$ are not plotted because the minimization leads to a non-physical solution (negative masses).

The analysis has been repeated considering the same refinement patterns but with no particle in the centre. In Figure 3 the minimum global density error is shown for all stencils. Comparing with Figure 2 for each pair of given values of ϵ and α, the global error obtained without the particle in the centre is always larger than the one obtained with that particle. Therefore, regardless of the refinement pattern considered, it is always an advantage to retain one particle in the centre.

Clearly the best splitting stencil is the one that produces the smallest global density error, so, looking at the maps plotted in Figure 2 all the four

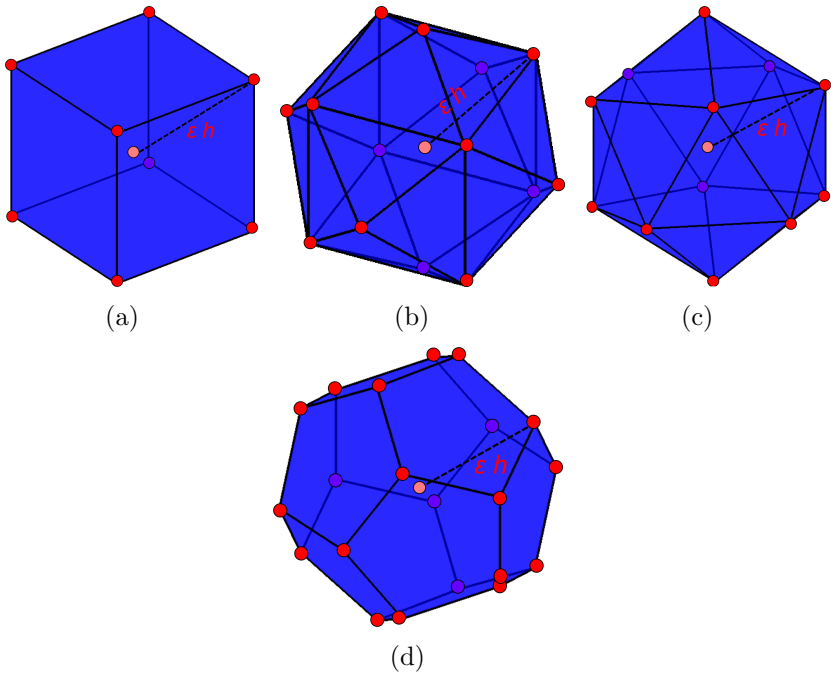

Figure 1: Refinement patterns: (a) cubic - 8 vertices, (b) cubic with additional vertex on faces - 14 vertices (c) Icosahedron - 12 vertices and (d) Dodecahedron - 20 vertices

refinement patterns considered have similar minimum values. However, for given values of α and ϵ the cubic+1 stencil produces larger error (Figure 2-a), which should be avoided. The global density error produced by the other three stencils (Figure 2-c, e and g) are similar, but the icosahedron+1 achieves this with the minimum number of daughter particles (Figure 2-e). This means that the number of neighbours for a given split particle is minimised if the icosahedron+1 stencil is used and thus this stencil produces the maximum efficiency. For this reasons the icosahedron+1 stencil is adopted in this work.

The analysis described above has been conducted using the Wendland kernel. To assess if the choice of the kernel influences the global density error and the mass distribution, the icosahedron+1 refinement pattern, with one particle in the centre, has also been analysed using the cubic and the quintic spline kernels. Results are plotted in Figures 4 and 5. For given α and ϵ values both the cubic and the quintic spline kernels produce a slightly smaller global density error $\mathscr{E}^*$, in comparison with the Wendland kernel

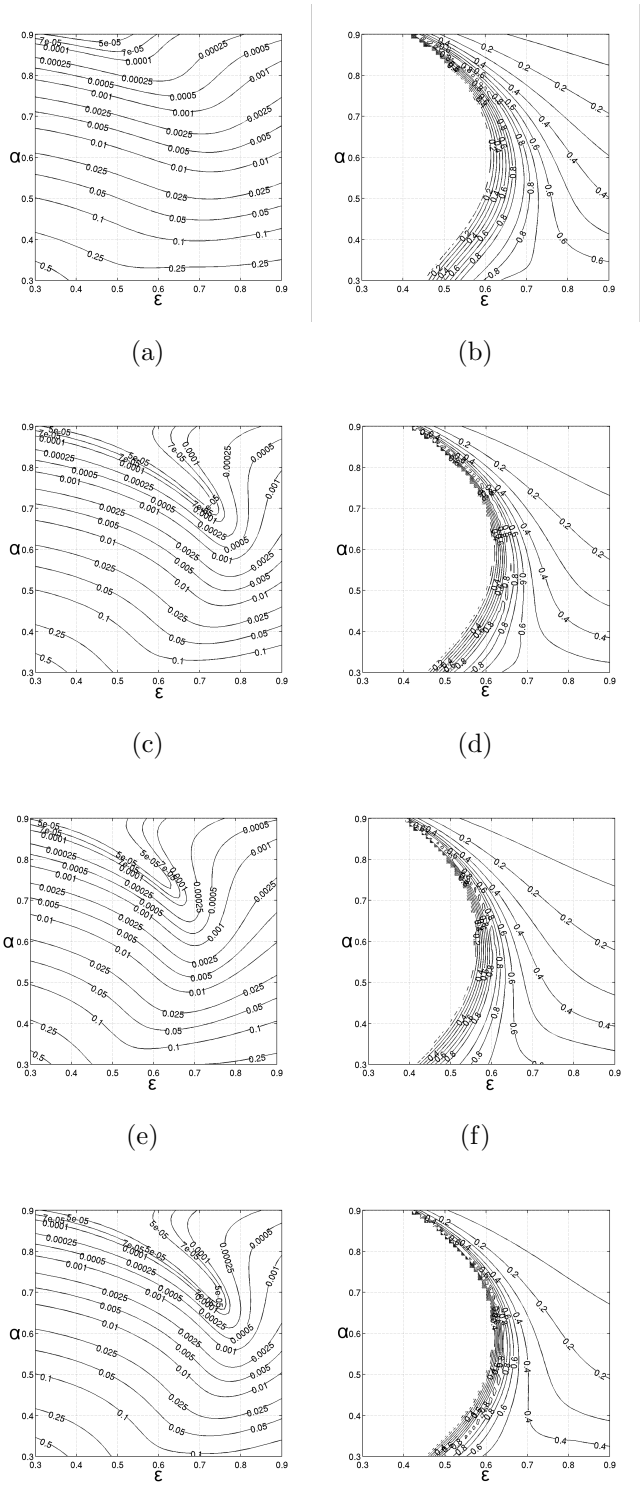

Figure 2: Error analysis of different stencils using Wendland kernel, left column shows global density error, and right column shows the mass ratio contours $\lambda_{min}/\lambda_{max}$. First Row, (a) and (b): cubic stencil of 8+1 particles. Second Row, (c) and (d): cubic stencil of 14+1 particles. Third row, (e) and (f): icosahedron+1 stencil. Fourth row, (g) and (h): dodecahedron+1 stencil.

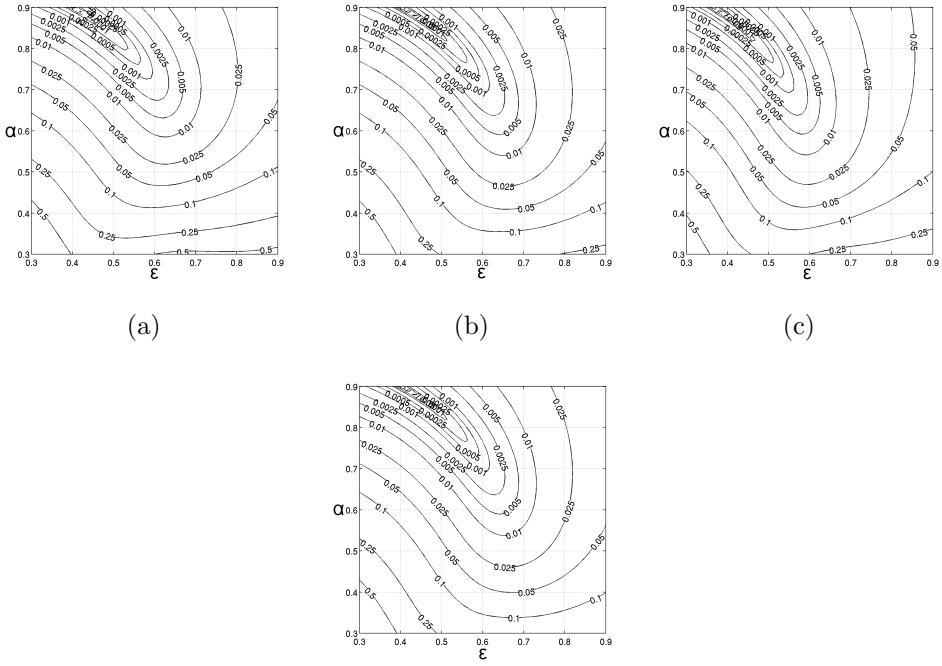

(a) (b) (c)

(d)

Figure 3: Density error contour with Wendland kernel *without* particle in the centre: (a) cubic stencil - 8 vertices, (b) cubic stencil - 14 vertices, (c) Icosahedron, (d) Dodecahedron

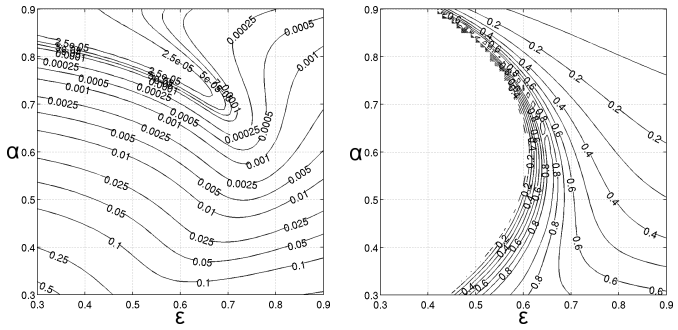

Figure 4: Icosahedron+1 stencil with Cubic kernel: global density error (a) and $\lambda_{min}/\lambda_{max}$ (b)

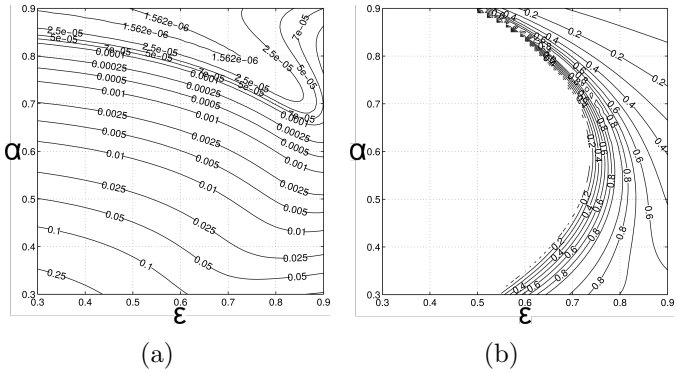

Figure 5: Icosahedron+1 stencil with quintic spline kernel: (a) global density error and (b) $\lambda_{min}/\lambda_{max}$

results shown in Figure 2. However both the global density error and the ratio between the minimum and maximum masses $\lambda_{min}/\lambda_{max}$ are similar to the one obtained using the Wendland kernel (shown in Figure 2).

In Table 1 the minimum error for different example values of α and ϵ is shown using the icosahedron+1 pattern and the Wendland kernel, Tables 2 and 3 show the same values considering the cubic and the quintic spline kernels confirming the error from these two kernels is slightly smaller. In Figures 6-8 the comparison between the orignal kernel functions and their reconstructions obtained using the daughter particles is plotted along one radial direction. The reconstruction for the kernel W_{rec} and the kernel gradient

Table 1: global density errors $\mathscr{E}^*$, and $\frac{\lambda_{min}}{\lambda_{max}}$ obtained considering different values of α and ϵ with the Icosahedron stencil and the Wendland kernel

ϵ	α	$\mathscr{E}^*$	$\frac{\lambda_{min}}{\lambda_{max}}$
0.70	0.70	1.754e-04	0.23
0.65	0.70	8.326e-05	0.33
0.60	0.70	2.969e-04	0.57
0.57	0.70	5.572e-04	0.91
0.60	0.75	5.602e-05	0.36

Table 2: global density errors $\mathscr{E}^*$, and $\frac{\lambda_{min}}{\lambda_{max}}$ obtained considering different values of α and ϵ with the Icosahedron stencil and the Cubic kernel

ϵ	α	$\mathscr{E}^*$	$\frac{\lambda_{min}}{\lambda_{max}}$
0.65	0.70	6.5932e-5	0.56
0.70	0.70	5.761e-5	0.33
0.62	0.70	1.637e-4	0.99
0.59	0.75	2.589e-5	0.99

∇W_{rec} at generic position $\mathbf{x}$ is obtained as follows:

$$\begin{aligned} W_{rec}\left(\mathbf{x}\right) &= \sum_{j}^{M_S} W_j\left(\mathbf{x}, h_j\right) \lambda_j \\ \nabla W_{rec}\left(\mathbf{x}\right) &= \sum_{j}^{M_S} \nabla W_j\left(\mathbf{x}, h_j\right) \lambda_j \end{aligned} \tag{8}$$

The optimal values of $\alpha = 0.70$; $\epsilon = 0.65$ have been used for the Wendland and the cubic spline and $\alpha = 0.70$; $\epsilon = 0.75$ for the quintic spline kernels. Using non-optimal values does not produce such close agreement for unrefined and refined kernel estimates.

4. Particle coalescing

To recover the initial resolution when the smaller particles leave the fine resolution region a particle coalescing (or merging) algorithm is developed. As presented in 2D [23] the coalescing is operated in pairs, between particles a (small one) and b, the latter one being defined as the particle with the

Table 3: global density errors $\mathscr{E}^*$, and $\frac{\lambda_{min}}{\lambda_{max}}$ obtained considering different values of α and ϵ with the Icosahedron stencil and the Quintic spline kernel

ϵ	α	$\mathscr{E}^*$	$\frac{\lambda_{min}}{\lambda_{max}}$
0.84	0.70	2.856e-5	0.35
0.72	0.70	2.637e-4	0.32
0.75	0.70	1.694e-4	0.98
0.71	0.75	4.907e-5	0.90

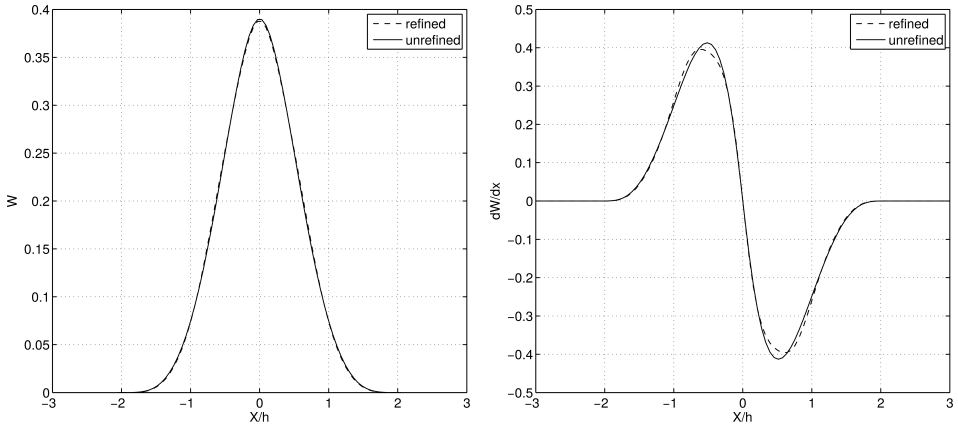

(a) (b)

Figure 6: Icosahedron+1 stencil, Wendland kernel with α=0.7 and ϵ=0.65: kernel shape (a) and kernel derivative (b) with Wendland kernel

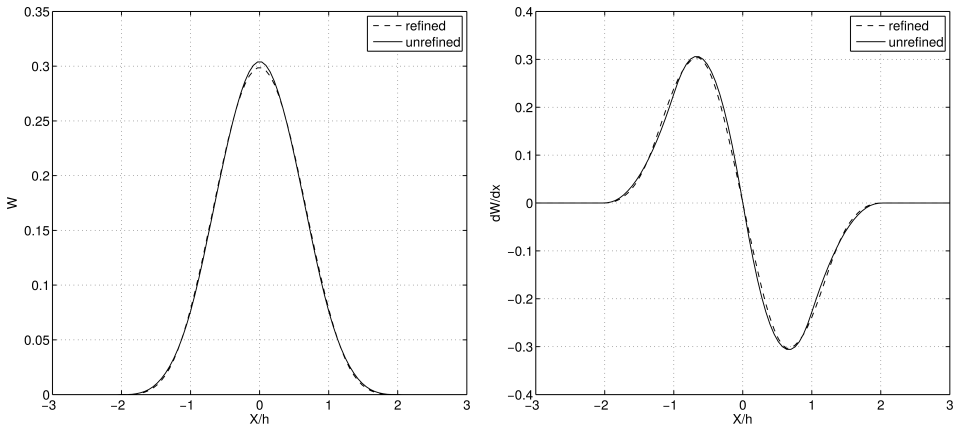

(a) (b)

Figure 7: Icosahedron stencil+1, Cubic kernel with α=0.7 and ϵ=0.65: kernel shape (a) and kernel derivative (b)

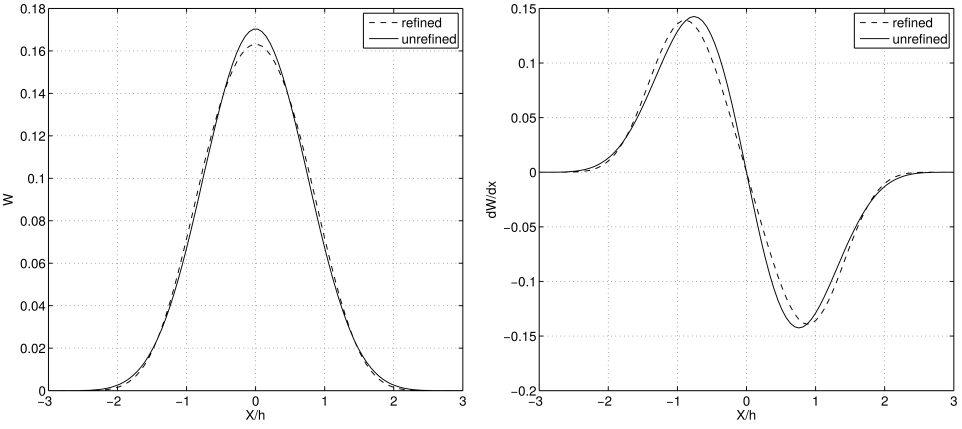

(a) (b)

Figure 8: Icosahedron+1 stencil, Quintic spline kernel with α=0.7 and ϵ=0.75: kernel shape (a) and kernel derivative (b)

minimum distance from the former one. The two particles are coalesced into a new larger particle, M_C. If the the new particle M_C is still too small, then it can be coalesced in the next time step, but no further particles are coalesced with M_C in the same time step. By imposing the mass and momentum conservation the mass m_{M_C} position $\mathbf{x}_{M_C}$ and velocity $\mathbf{v}_{M_C}$ of the new particle are calculated as:

$$m_{M_C} = m_a + m_b \tag{9}$$

$$\mathbf{x}_{M_C} = \frac{m_a \mathbf{x}_a + m_b \mathbf{x}_b}{m_{M_C}}, \tag{10}$$

$$\mathbf{v}_{M_C} = \frac{m_a \mathbf{v}_a + m_b \mathbf{v}_b}{m_{M_C}}. \tag{11}$$

The smoothing length of the new particle h_{M_C} is derived by imposing that the density at position $\mathbf{x}_{M_C}$ remains constant [23]. After coalescing the density error e at $\mathbf{x}_{M_C}$ is equal to:

$$\begin{aligned} e(\mathbf{x}_{M_C}) &= m_{M_C} W_{M_C,M_C} - [m_a W_{M,a} \\ &\quad + m_b W_{M,b}] \end{aligned} \tag{12}$$

where $W_{M_C,a} = W(\mathbf{x}_a - \mathbf{x}_{M_C}, h_a)$, $W_{M_C,b} = W(\mathbf{x}_b - \mathbf{x}_{M_C}, h_b)$ and $W_{M_C,M_C} = W(0, h_{M_C})$. The only unknown is the smoothing length of the new particle h_{M_C} which can be calculated by imposing that no density error is introduced at $\mathbf{x}_{M_C}$, this means that $e(\mathbf{x}_{M_C}) = 0$. If the Wendland kernel is adopted h_{M_C} is equal to:

$$h_{M_C} = \left(\frac{16\pi}{21} \frac{m_{M_C}}{m_a W_{M,a} + m_b W_{M,b}} \right)^{1/3} \tag{13}$$

Analogous equations can be easily derived if a different kernel is adopted.

5. SPH formulation

We now demonstrate how this dynamic particle refinement scheme performs in 3-D simulations. First the conservative variationally consistent formulation is presented. In this work we follow the classical approach of slight compressibility adopted in many SPH numerical schemes. Mass and

momentum conservation for a pseudo-compressible fluid, can be written in Lagrangian form as:

$$\frac{\mathrm{d}\rho}{\mathrm{d}t} = -\rho\nabla\cdot\mathbf{v} \tag{14}$$

$$\frac{\mathrm{d}\mathbf{v}}{\mathrm{d}t} = -\frac{1}{\rho}\nabla p + \nu_0\nabla^2\mathbf{v} + \mathbf{g} \tag{15}$$

where ρ is the fluid density, $\mathbf{v}$ is the velocity vector, p is the pressure, g is the gravity acceleration and ν_0 is the kinematic viscosity.
The two equations are coupled by means of an equation of state commonly referred to as Tait's:

$$p = p_0 + B\left[\left(\frac{\rho}{\rho_0}\right)^{\gamma} - 1\right] \tag{16}$$

where γ is a constant taken equal to 7 as suggested by different authors [12, 7], $\rho_0 = 1000$ kg/m^3 is the reference density, p_0 is initial background pressure and $B = c_0^2\rho_0/\gamma$ where c_0 is the speed of sound in the fluid. The speed of sound is conveniently reduced to obtain a larger computational timestep. In this work the speed of sound is defined as $c_0 = 10U_{max}$ where U_{max} is the maximum expected fluid velocity. The equations are integrated in time using the sympletic scheme [13], and the time-step is defined according to the Courant-Friedrich-Levy condition as reported in [14]. The formulation herein adopted has been derived in [23] and it is only briefly recalled here.
The SPH discretization of Equation (14) is:

$$\frac{\mathrm{d}\rho}{\mathrm{d}t} = -\rho_i\sum_j \frac{m_j}{\rho_j}\left(\mathbf{v}_j - \mathbf{v}_i\right)\cdot\nabla W_j\left(x_i, h_j\right) \tag{17}$$

whereas the pressure gradient term of Equation (15) is discretized as follows:

$$\frac{1}{\rho}\nabla p = \sum_j \frac{m_j}{\rho_j\rho_i}\left[p_i\nabla W_j\left(x_i, h_j\right) - p_j\nabla W_i\left(x_j, h_i\right)\right] \tag{18}$$

please note that, in case of particles with constant smoothing length h, $\nabla W_j\left(x_i, h\right) = \nabla W_i\left(x_j, h_i\right)$ and thus Equation (18) becomes:

$$\frac{1}{\rho}\nabla p = \sum_j \frac{m_j}{\rho_j\rho_i}\left(p_i + p_j\right)\nabla W_j\left(x_i, h_j\right) \tag{19}$$

which is one of the classical formulations of the pressure gradient term used in SPH models with constant resolution. Both Equations (18) and (19) satisfy the action-reaction principle and thus guarantee the momentum conservation. According to [4] this formulation ensures conservation and satisfies the principle of virtual work for free-surface flows. Therefore, although no consistency of the pressure gradient is ensured close to the the free surface, it can also be successfully applied to free-surface flows without any special treatment of the free surface.
Finally, the SPH discretization of the laminar viscosity term is discretized as:

$$\nu_0 \nabla^2 \mathbf{v} = \sum_j m_j \left[\frac{4\nu_0 r_{ij} \nabla \bar{W}_{ij}}{\rho_{ij} r_{ij}^2} \right] \mathbf{v}_{ij} \tag{20}$$

where ν_0 is the kinematic viscosity of the fluid, $r_{ij} = |\mathbf{x}_i - \mathbf{x}_j|$, $\mathbf{v}_{ij} = \mathbf{v}_i - \mathbf{v}_j$, $\rho_{ij} = 0.5\left(\rho_i + \rho_j\right)$, and $\nabla \bar{W}_{ij} = 0.5\left[\nabla W_j\left(\mathbf{x}_i, h_j\right) + \nabla W_i\left(\mathbf{x}_j, h_i\right)\right]$.
A diffusivity term has been added to the continuity equation in order to improve the stability of the numerical scheme, as suggested by Molteni & Colagrossi [11], Equation (17) is therefore modified as follows:

$$\begin{aligned} \frac{\mathrm{d}\rho}{\mathrm{d}t} = -\rho_i \sum_j \frac{m_j}{\rho_j} \left(\mathbf{v}_j - \mathbf{v}_i\right) \cdot \nabla W_j\left(x_i, h_j\right) + \\ \xi h_i c_0 \sum_j \frac{m_j}{\rho_j} \psi_{ij} \nabla W_j\left(x_i, h_j\right) \end{aligned} \tag{21}$$

where ξ is the artificial density diffusion parameter, assumed equal to 0.1, c_0 is the reference speed of sound and the term ψ_{ij} is defined as:

$$\psi_{ij} = \left(\frac{\rho_j}{\rho_i} - 1 \right) \frac{\mathbf{x}_i - \mathbf{x}_j}{r_{ij}^2 + 0.01 h_i^2} \tag{22}$$

To prevent errors created by irregular particle distributions the shifting formulation presented in [19] for an incompressible SPH (ISPH) scheme has been applied herein to the variable-h weakly compressible SPH scheme.
Boundary conditions are enforced using the fixed ghost particle method [10], the analysis of dynamic particle refinement in the vicinity of the boundary is beyond the scope of the present work. Following from the analysis in Section 3, the Wendland kernel has been adopted, and the splitting is operated with $\alpha = 0.7$ and $\epsilon = 0.65$.

6. Test Cases

6.1. Error analysis of SPH interpolation

To assess the error produced by the SPH interpolation in the presence of particles with different sizes a theoretical test case has been set up with a cube domain where the numerical effect of splitting and coalescing with the optimal patterns from Section 3 can be quantified. On each face of the cube a non-slip wall boundary condition has been imposed, thus no free surface is present. Please note also that no gravity or any other external forces has been considered. In [16] a similar test case was run in 2-D with the aim of assessing how particles rearrange themselves if the formulation ensures momentum conservation. In the present work this test case has two different purposes: (i) to verify if the variable-resolution formulation adopted here is also able to preserve the same particle re-arranging capability and behaviour, and (ii) to assess the errors produced by particle splitting / coalescing. Hence, the presence of particles with different masses is compared with the error of the same simulation using uniform resolution. This test case has been run with three different set-ups: (i) no adaptivity, (ii) splitting and no coalescing, and (iii) with coalescing activated in the centre of the domain, but no splitting in that region.

The side of the cube domain is of length $L = 1m$ and the initial size of the particles Δx_0 is equal to $0.05m$. Particle positions have been defined using a pseudo-random distribution (as used in [25]) in the central part of the domain with standard deviation equal to $0.1\Delta x_0$. To trigger particle movements the initial background pressure p_0 has been assumed equal to 1000 Pa and the kinematic viscosity $\nu = 0.01$. The reference velocity for this simulation is equal to $\sqrt{p_0/\rho_0}$, the Reynolds number is $Re = 1/\nu = 100$.
The variable resolution is defined according to the minimum and maximum values of pre-specified resolution: Δx_{min} and Δx_{max}: one particle i is split if its resolution $\Delta x_i = (m_i/\rho_i)^{1/3}$ is bigger than Δx_{max}. Similarly, a particle is coalesced if $\Delta x_i < \Delta x_{min}$. Δx_{min} and Δx_{max} have been defined in the central part of the domain when $0.3L < (x,y,z) < 0.7L$ as described in Table 4, whereas $\Delta x_{max} = \infty$ and $\Delta x_{min} = 0$ everywhere else.

Splitting is operated using the icosahedron+1 stencil, with $\epsilon = 0.65$ and $\alpha = 0.7$. Masses of the daughter particles obtained from the error minimization procedure described in Section 3.1 which leads to the mass distribution for the daughter particles reported in the second row of Table 1.

Table 4: definition of Δx_{min} and Δx_{max} in central part of the domain $0.3L < x, y, z < 0.7L$ for the three different set-up of Error analysis simulation

Simulation	Δx_{max}	Δx_{min}
(i) no adaptivity	$\Delta x_{max} = \infty$	$\Delta x_{min} = 0$
(ii) only splitting	$\Delta x_{max} = 0.5\Delta x_0$	$\Delta x_{min} = 0$
(iii) only coalescing	$\Delta x_{max} = \infty$	$\Delta x_{min} = 1.01\Delta x_0$

Particles are coalesced using the procedure described in section 4. In both simulations the 3-D Wendland kernel is adopted with initial smoothing length $h_0 = 1.5\Delta x_0$.

In Figure 9 L_2 norms of (a) velocity magnitude and (b) non-dimensional density errors are plotted against time, whereas the velocity magnitude is plotted in Figure 10 at time 2 s. The distribution of the velocity magnitude shown in cut-out cross-sections in Figure 10 confirms that the largest error is produced in the centre of the domain where the particle refinement occurs and that coalescing generates the largest velocity error. The maximum velocities are on the order of 0.001 m/s which is 0.1% of the characteristic velocity $\sqrt{p_0/\rho_0}$. As expected, in all three set-ups the error norms are reducing in time, meaning that the formulation adopted is able to ensure particle rearrangements also in presence of particles with different sizes. The larger initial errors for the simulation with splitting (ii) are due to the fact that particle splitting creates a highly non-uniform particle distribution, but as the simulation evolves, particles are able to rearrange themselves reducing the error. After particle rearrangement, the simulation (ii) with finer resolution has smaller density and velocity errors, this demonstrates that the particle splitting procedure does not introduce any significant error, and conversely is able to increase the resolution and thus to reduce the errors both in the velocity and density field. Conversely the simulation (iii) where the resolution was reduced in the central part of the domain produced the larger errors as expected.

6.2. Poiseuille Flow

The results obtained with the proposed numerical scheme are here compared against the analytical solution of 3-D Poiseuille flow. Periodic boundary conditions are used in the y-direction which is also the direction of the flow. The pipe diameter D and pipe length L_y are set equal to 1 m and 0.5 m respectively and the initial particle size of the particles Δx_0 is equal to

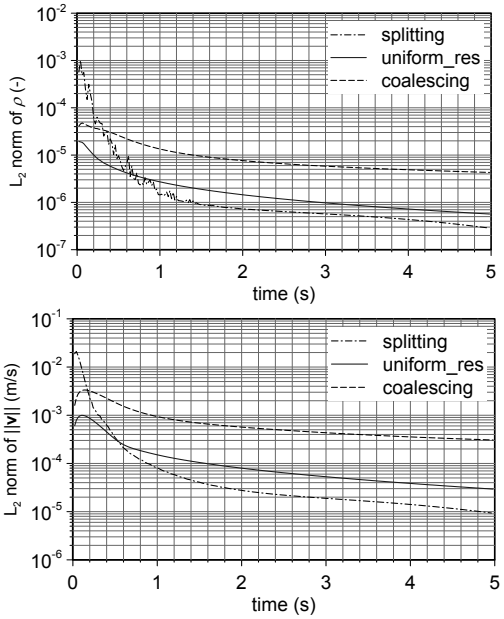

Figure 9: Error analysis simulation: L_2 norms of (a) velocity magnitude and (b) non-dimensional density errors

0.025 m. The cylindrical symmetry axis of the pipe is $y = y_0$, the Reynolds number is defined as $Re = U_{max}D/\nu$ where U_{max} is the maximum velocity which occurs in the centreline of the domain and ν is the water kinematic viscosity. Assuming $U_{max} = 1$ m/s then $Re = 1/\nu$. A periodic boundary condition is applied in the y direction. As explained in the previous test case one particle i is split if its resolution $\Delta x_i = (m_i/\rho_i)^{1/3}$ is bigger than Δx_{max}. Similarly it is coalesced if $\Delta x_i < \Delta x_{min}$. To activate particle splitting and coalescing the following different zones have been defined in the domain:

1. in the portion of the domain $0< y < 0.5L_y$, and $r < 0.9D$ $\Delta x_{max} = \infty$ and $\Delta x_{min} = \Delta x_0$.
2. In the area $0.5\ L_y < y < L_y$ and $r < 0.9D$, $\Delta x_{max} = \Delta x_0$ and $\Delta x_{min} = 0$ (this means no particle coalescing and particle splitting).

with r the distance between the particle and the $y = y_0$ axis. In this way particles are continuously split and coalesced during the simulation. In this work, the particle refinement operations of splitting and coalescing do not occur as blocks of particles as suggested by other authors [2]. Instead, splitting and coalescing can occur in specified regions subject to specific criteria

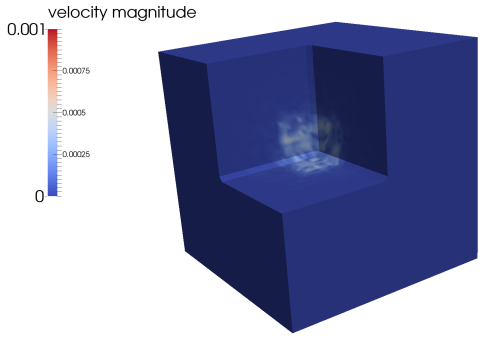

(a)

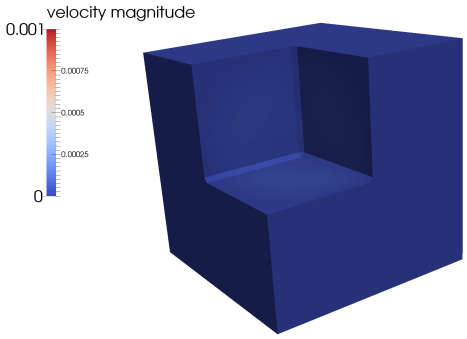

(b)

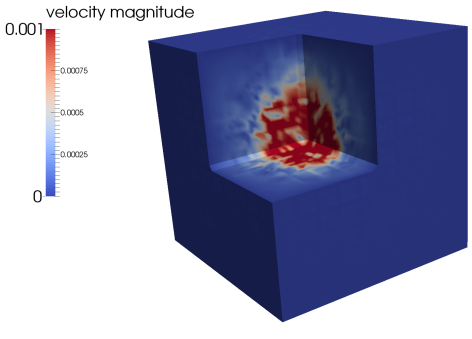

(c)

Figure 10: Error analysis simulation: velocity magnitude (m/s) at time 2 s for three different set-ups: (a) no adaptivity, (b) only splitting and (c) only coalescing

Table 5: Pouseuille flow with Re=10, 100 and 1000 L_2 norm of the v_y error

Δx_0	$Re = 10$	$Re = 100$	$Re = 1000$
0.05 m	8.05e-03	7.41e-03	3.03e-02
0.025 m	2.26e-03	3.01e-03	7.98e-03
0.0125 m	1.01e-03	7.57e-04	2.11e-03
Rate of conv.	1.54	1.64	1.92

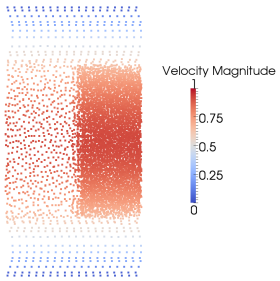

Figure 11: Pouseuille flow for Re=100, particle position and velocity magnitude (m/s)

such as ones specified above. Three simulations have been performed for $Re = 10,\ 100,\ 1000$. In Table 5 the L_2 norm of the v_y error for each Re is calculated considering all particles in the domain. The rate of convergence is always bigger than 1.5 and it is increasing with Re. Figure 11 shows the velocity magnitude and the particle position for Re=100, both high and low resolution zones are clearly visible, and continuous particle splitting and coalescing are able to increase and decrease the size of the particle in the prescribed zones.
In Figure 12 the v_y velocity profile along radial direction at $y = 0.25m$ is plotted for different Reynolds numbers of 10,100, 1000. The results are in good agreement with the analytical solution and no significant spurious oscillations are present in the velocity profiles although the particles are split and coalesced multiple times.

6.3. 3-D lid-Driven cavity flow

The lid-driven-cavity problem is one of the fundamental benchmarks not only for SPH models but for every kind of Navier-Stokes numerical schemes. The domain is a cube (a square in 2D) and the flow is driven by the tangential motion of a single lid. Despite the simple geometry, the flow develops fully

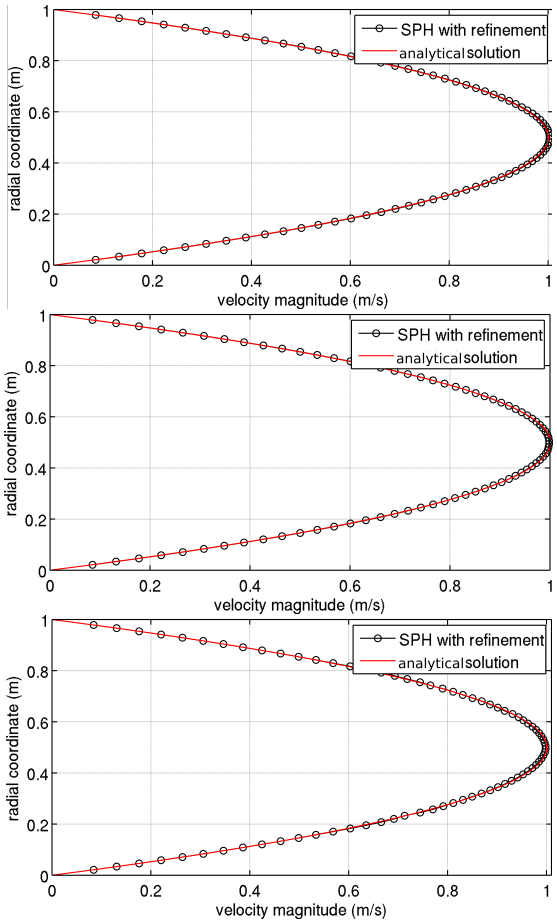

Figure 12: Pouseuille flow $\Delta x = 0.025$ m and $Re = 10$ (a), 100 (b) and 1000 (c), v_y values at section x= 0.025 with refinement

3-D vortices. In this work, to the best of the authors' knowledge, the 3-D lid-driven cavity flow [1] is simulated here with Reynolds numbers Re = 100, 400 and 1000 for the first time with SPH. As shown in Figure 13, a cube with length side L =1 m has been considered, and with the velocity of the lid given by $\mathbf{U}_{lid}$ =(1,0,0) m/s. To assess the performance of the 3-D splitting and coalescing schemes, higher resolution is adopted close to the walls and particles are split when they leave the central part of the domain and coalesced if they enter in the central part the domain. Therefore, two different resolution zones have been defined:

1. in the region close to the walls (distance from a fluid particle to the wall is less than 0.2 m) the maximum particle size has been set equal to Δx_{max} = 0.05, 0.025 and 0.0125 m for Re =100, 400 and 1000 respectively, and $\Delta x_{min} = 0$.
2. in the region far from the walls (distance from a fluid particle to the wall is greater than 0.2 m) the particle size has been set equal to Δx_{min} =0.08, 0.04 and 0.02 m for Re =100, 400 and 1000 respectively, and $\Delta x_{max} = \infty$.

Figure 14 displays the velocity magnitude and the particle position for Re=400 showing that particle splitting is effective in increasing the resolution close to the boundaries while a coarser resolution is recovered in the central part of the domain by means of particle coalescing. Figure 15 shows the velocity vector for Re=400 on a vertical section at y=0.5 m, both the primary vortex in the central part of the domain and secondary one in the lower right corner are clearly visible. In Figure 16 the results for Re = 100, 400 and 1000 are compared against the reference solutions obtained in [1] with a high-order finite difference scheme. Specifically, the velocities v_x and v_z non-dimensionalized with respect to the lid velocity in the x-direction are compared along lines (0.5,0.5,z/L) and (x/L,0.5,0.5) respectively. The agreement with the reference solution is satisfactory, and the numerical model is able to reproduce the 3-D characteristics of the flow.

7. Conclusion

In this paper a 3-D parallel weakly compressible SPH numerical scheme with particle splitting and coalescing procedures has been presented. This enables 3-D SPH simulation with dynamically adaptive variable resolution such that the error in density is minimised conserving both mass and momentum.

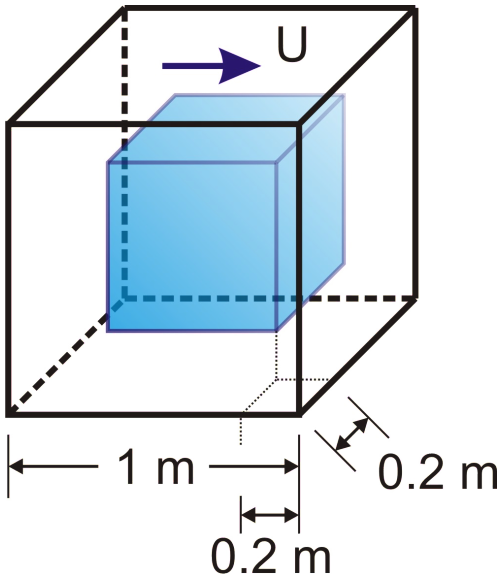

Figure 13: 3-D lid driven cavity flow: lower resolution zone in the center (in blue) and high resolution close to the boundaries

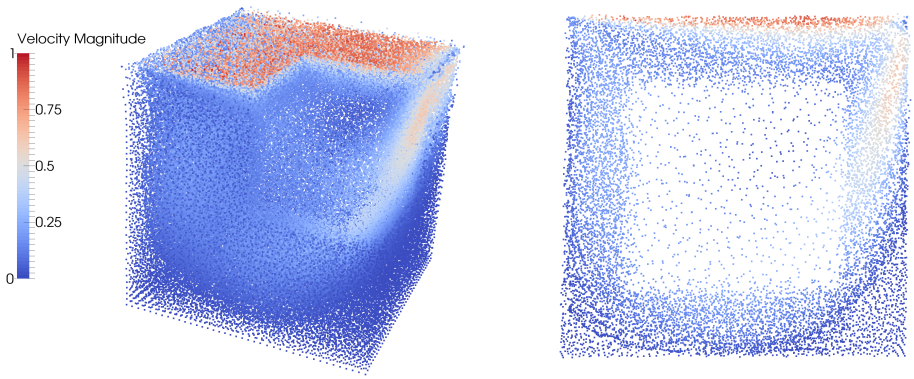

Figure 14: 3-D lid driven cavity flow for Re=400, velocity magnitude (m/s) in 3D (a) and on a vertical section at y=0.5 m (b)

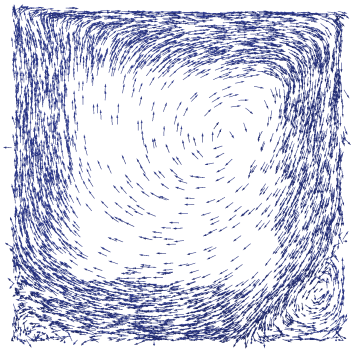

Figure 15: 3-D lid driven cavity flow for Re=400, velocity vectors on a vertical section at y=0.5 m

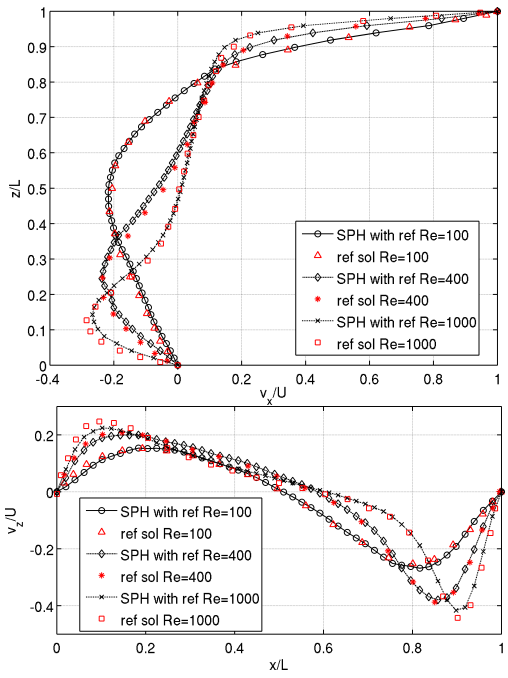

Figure 16: 3-D lid driven cavity flow, $v_x/U_{x,lid}$ on the line (0.5,0.5,z/L) (a) and $v_z/U_{x,lid}$ on the line (x/L,0.5,0.5) (b)

In comparison to 2-D approaches, there is a greater number of degrees of freedom in 3D with the variables that influence the choice of optimal solution, and this includes the particle arrangements and the smoothing lengths of the daughter particles. Following on from work in 2D, an *a priori* error minimisation approach has been used to define the optimal mass distribution of the daughter particles before the beginning of the simulation. We have analysed 4 different splitting arrangements for the daughter particles: (i) a cubic stencil with 8 particles, (ii) a cubic stencil plus 6 additional particles located on a sphere co-inciding with the cubic face centres, (iii) an icosohedron-shaped arrangement with 14 particles, and (iv) a dodecahedron-shaped arrangement with 20 particles. The analysis for each splitting arrangement was repeated with and without a daughter particle at the centre of the arrangement. An analysis of different 3-D splitting stencils has been conducted by investigating the minimum global density error and the efficiency of the numerical scheme. It has been demonstrated that:

- The icosahedron+1 is the optimal refinement stencil;
- Regardless of the stencil adopted, to minimize the density error a daughter particle should be placed at the same position of the original particle;
- Different kernels produce similar density errors, so the optimal refinement stencil is independent of the kernel adopted.

In addition to the splitting procedure and analysis, a new 3-D coalescing procedure for the coalescing of SPH particles into a new single particle has been presented. A simple test case looking at the error introduced into a simulation either solely from splitting or coalescing confirmed that the finer resolution reduces the error within the simulation. The accuracy of the new formulation was then tested against reference solutions for 3-D Poiseuille flow and a 3-D Lid-driven cavity flow, for a range of different Reynolds numbers. Similar to 2D, further research is needed to assess appropriate adaptivity criteria for particle splitting and coalescing for more general applications to ensure a uniform error distribution.

[1] S. Albensoeder and H. Kuhlmann. Accurate three-dimensional lid-driven cavity flow. *Journal of Computational Physics*, 206(2):536 – 558, 2005.

[2] D. Barcarolo, D. L. Touzé, G. Oger, and F. de Vuyst. Adaptive particle refinement and derefinement applied to the smoothed particle hydrodynamics method. *Journal of Computational Physics*, 273(0):640 – 657, 2014.

[3] S. Børve, M. Omang, and J. Trulsen. Regularized smoothed particle hydrodynamics with improved multi-resolution handling. *Journal of Computational Physics*, 208(1):345 – 367, 2005.

[4] A. Colagrossi, M. Antuono, and D. Le Touzé. Theoretical considerations on the free-surface role in the smoothed-particle-hydrodynamics model. *Phys. Rev. E*, 79:056701, May 2009.

[5] J. Feldman and J. Bonet. Dynamic refinement and boundary contact forces in sph with applications in fluid flow problems. *International Journal for Numerical Methods in Engineering*, 72(3):295–324, 2007.

[6] O. fundation. Openfoam website, April 2014.

[7] M. Gomez-Gesteira, B. D. Rogers, R. A. Dalrymple, and A. J. Crespo. State-of-the-art of classical sph for free-surface flows. *Journal of Hydraulic Research*, 48(sup1):6–27, 2010.

[8] L. Hernquist and N. Katz. Treesph- a unification of sph with the hierarchical tree method. *The Astrophysical Journal*, 70:419–446, 1989.

[9] M. Lastiwka, N. Quinland, and B. M. Adaptive particle distribution for smoothed particle hydrodynamics. *International Journal for Numerical Methods in Fluids*, 47(10–11):1403–1409, 2005.

[10] S. Marrone, A. Colagrossi, M. Antuono, G. Colicchio, and G. Graziani. An accurate {SPH} modeling of viscous flows around bodies at low and moderate reynolds numbers. *Journal of Computational Physics*, 245(0):456 – 475, 2013.

[11] D. Molteni and A. Colagrossi. A simple procedure to improve the pressure evaluation in hydrodynamic context using the sph. *Computer Physics Communications*, 180(6):861 – 872, 2009.

[12] J. J. Monaghan. Simulating free surface flows with SPH. *Journal of Computational Physics*, 110:399–406, 1994.

[13] J. J. Monaghan. Smoothed particle hydrodynamics. *Reports on Progress in Physics*, 68:1703–1759, 2005.

[14] J. J. Monaghan and A. Kos. Solitary waves on a cretan beach. *Journal of Waterway, Port, Coastal, and Ocean Engineering*, 125(3):145–155, 1999.

[15] S. Popinet. Gerris: a tree-based adaptive solver for the incompressible euler equations in complex geometries. *Journal of Computational Physics*, 190(2):572 – 600, 2003.

[16] D. J. Price. Smoothed particle hydrodynamics and magnetohydrodynamics. *Journal of Computational Physics*, 231(3):759 – 794, 2012. Special Issue: Computational Plasma Physics Special Issue: Computational Plasma Physics.

[17] N. J. Quinlan, L. Lobovsk, and R. M. Nestor. Development of the meshless finite volume particle method with exact and efficient calculation of interparticle area. *Computer Physics Communications*, 185(6):1554 – 1563, 2014.

[18] Y. Reyes López, D. Roose, and C. Recarey Morfa. Dynamic particle refinement in sph: application to free surface flow and non-cohesive soil simulations. *Computational Mechanics*, 51(5):731–741, 2013.

[19] A. Skillen, S. Lind, P. K. Stansby, and B. D. Rogers. Incompressible smoothed particle hydrodynamics (sph) with reduced temporal noise and generalised fickian smoothing applied to bodywater slam and efficient wavebody interaction. *Computer Methods in Applied Mechanics and Engineering*, 265(0):163 – 173, 2013.

[20] F. Spreng, D. Schnabel, A. Mueller, and P. Eberhard. A local adaptive discretization algorithm for smoothed particle hydrodynamics. *Computational Particle Mechanics*, 1(2), 2014.

[21] C. Ulrich, N. Koliha, and T. Rung. Sph modelling of water/soil-flows using a variable resolution scheme. In *Proc. 6th ERCOFTAC SPHERIC workshop*, pages 101–108, Hamburg, Germany, 2011.

[22] R. Vacondio, B. Rogers, P. Stansby, and P. Mignosa. Shallow water SPH for flooding with dynamic particle coalescing and splitting. *Advances in Water Resources*, 58(0):10 – 23, 2013.

[23] R. Vacondio, B. Rogers, P. Stansby, P. Mignosa, and J. Feldman. Variable resolution for SPH: A dynamic particle coalescing and splitting scheme. *Computer Methods in Applied Mechanics and Engineering*, 256(0):132 – 148, 2013.

[24] R. Vacondio, B. D. Rogers, and P. K. Stansby. Accurate particle splitting for smoothed particle hydrodynamics in shallow water with shock capturing. *International Journal for Numerical Methods in Fluids*, 69(8):1377–1410, 2012.

[25] R. Vacondio, B. D. Rogers, and P. K. Stansby. Smoothed particle hydrodynamics: Approximate zero-consistent 2-d boundary conditions and still shallow-water tests. *International Journal for Numerical Methods in Fluids*, 69(1):226–253, 2012.